

## Comparison of gradient and flux driven gyro-kinetic turbulent transport

Cite as: Phys. Plasmas **23**, 052309 (2016); <https://doi.org/10.1063/1.4952621>

Submitted: 11 February 2016 • Accepted: 12 May 2016 • Published Online: 25 May 2016

F. Rath, A. G. Peeters, R. Buchholz, et al.



[View Online](#)



[Export Citation](#)



[CrossMark](#)

### ARTICLES YOU MAY BE INTERESTED IN

**Comparisons and physics basis of tokamak transport models and turbulence simulations**  
Physics of Plasmas **7**, 969 (2000); <https://doi.org/10.1063/1.873896>

**Gyrokinetic simulation of collisionless trapped-electron mode turbulence**  
Physics of Plasmas **12**, 072309 (2005); <https://doi.org/10.1063/1.1947447>

**Gradient-driven flux-tube simulations of ion temperature gradient turbulence close to the non-linear threshold**

Physics of Plasmas **23**, 082517 (2016); <https://doi.org/10.1063/1.4961231>

Physics of Plasmas

Papers from 62nd Annual Meeting of the  
APS Division of Plasma Physics

Read now!

# Comparison of gradient and flux driven gyro-kinetic turbulent transport

F. Rath,<sup>1</sup> A. G. Peeters,<sup>1</sup> R. Buchholz,<sup>1</sup> S. R. Grosshauser,<sup>1</sup> P. Migliano,<sup>2</sup> A. Weikl,<sup>1</sup> and D. Strintzi<sup>1</sup>

<sup>1</sup>*Physics Department, University of Bayreuth, 95440 Bayreuth, Germany*

<sup>2</sup>*Aix-Marseille Université, PIIM UMR 7345, Marseille, France*

(Received 11 February 2016; accepted 12 May 2016; published online 25 May 2016)

Flux and gradient driven ion temperature gradient turbulence in tokamak geometry and for Cyclone base case parameters are compared in the local limit using the same underlying gyro-kinetic turbulence model. The gradient driven turbulence described using the flux tube model with periodic boundary conditions has a finite ion heat flux  $Q_i \approx 10n_0T_0\rho_*^2v_{th}$ , where  $n_0$  ( $T_0$ ) is the background density (temperature),  $\rho_* = \rho/R$  is the normalized Larmor radius,  $R$  is the major radius of the device, and  $v_{th}$  is the ion thermal velocity at the nonlinear threshold of the temperature gradient length for turbulence generation. Consequently, the gradient driven local transport model is unable to accurately describe heat fluxes below  $Q_i < 10n_0T_0\rho_*^2v_{th}$ , since no stationary fully developed turbulent state can be obtained. The turbulence in the flux driven case shows intermittent behaviour and avalanches for  $Q_i < 10n_0T_0\rho_*^2v_{th}$ . Isolated avalanches disappear for  $Q_i > 10n_0T_0\rho_*^2v_{th}$ , and at higher heat fluxes, the statistics of the turbulence is the same for the flux and gradient driven case. The nonlinear upshift of the temperature gradient length threshold for turbulence generation (known as the Dimits shift) is larger in the case of flux driven turbulence. This higher nonlinear upshift is attributed to the generation of structures in the radial temperature profile, known as staircases [Dif-Pradalier, Phys. Rev. E **82**, 025401 (2010)]. Avalanches are initiated at specific locations and have roughly the same radial extent of 50–70 ion Larmor radii. The staircases are obtained at low heating rates, and become unstable and break up at higher heating rates. At the heat fluxes for which staircase formation is observed, no stationary gradient driven simulations can be obtained. *Published by AIP Publishing.*

[<http://dx.doi.org/10.1063/1.4952621>]

## I. INTRODUCTION

Plasma confinement in fusion devices is set by turbulent transport. Due to the imposed magnetic field, the scale of the turbulent eddies perpendicular to the magnetic field is governed by the Larmor radius ( $\rho$ ), which is much smaller than the size of the device ( $R_0$ ). The smallness parameter  $\rho/R_0$  is useful in developing models that describe the turbulence, such as the gyro-kinetic framework, which is described in detail in the review of Ref. 1. Because of its importance for confinement and, therefore, for the ability of a fusion device to reach ignition, a large amount of literature is devoted to the topic. Increasingly important therein is the ability to simulate particle, heat, and momentum transport fluxes under experimentally relevant conditions.

In the limit of small normalized Larmor radius ( $\rho_* = \rho/R_0 \ll 1$ ), the turbulence is believed to be homogeneous and can be described in the local limit using a flux tube geometry with periodic boundary conditions in the plane perpendicular to the magnetic field. In this case, the background gradients of density, temperature, and rotation are specified, and the fluxes of particles, heat, and momentum are calculated. Although density, temperature, and momentum fluctuations exist in the computational domain, the average of these fluctuations over the domain is by definition zero and, consequently, the averaged gradients are equal to the specified background gradients. This setup is referred to as

gradient driven (GD) turbulence as one obtains the fluxes for specified gradients.

In the case of flux driven (FD) turbulence, the fluxes are prescribed and the gradients are allowed to freely adjust. This setup can be considered to be closer to the experimental situation, where the plasma is heated with a given power source. Nevertheless, in the limit of small normalized Larmor radius, one could expect both flux and gradient driven turbulence to give the same result, since the latter presents a consistent description valid in the  $\rho_* \rightarrow 0$  limit.

There is a vast amount of literature on both gradient as well as flux driven transport. Usually, the flux driven results presented in the literature go beyond the local limit approximation for which gradient driven results are obtained. Furthermore, different approximations in the model equations are being made, with flux driven results generally retaining profile physics, and gradient driven turbulence generally using a more sophisticated turbulence model. Because of these differences, a direct comparison between flux and gradient driven turbulence in the  $\rho_* \rightarrow 0$  limit has, to our knowledge, not been published.

In this paper, a direct comparison between gradient and flux driven turbulence is made. In order to obtain this comparison, the same turbulence model will be used in both cases, and furthermore, the flux driven cases are obtained in the local limit.

## II. NUMERICAL EXPERIMENTS

Below, the setup of the numerical experiments will be given in detail. The turbulence is described using the gyro-kinetic model<sup>1</sup> in the electro-static limit, with adiabatic electrons, and neglecting collisions as well as toroidal plasma rotation. The plasma parameters are taken from the Cyclone base case:<sup>2</sup> density gradient  $R/L_n = 2.2$ , safety factor  $q = 1.4$ , magnetic shear  $\hat{s} = 0.78$ , inverse aspect ratio  $\epsilon = 0.19$ , and electron to ion temperature ratio  $T_e/T_i = 1$ . The temperature gradient length  $R/L_T$  has been varied in the gradient driven simulations and allowed to adjust freely in the flux driven simulations. In contrast to many simulations described in Ref. 2 that use the  $\hat{s} - \alpha$  geometry, a geometry of circular concentric surfaces is used here, keeping all orders of the inverse aspect ratio.<sup>3</sup>

The numerical results are obtained with the flux tube version of the non-linear gyro-kinetic code GKW,<sup>4</sup> with the radial direction described by finite differences in order to allow for the radial inhomogeneity in the flux driven case. The flux driven simulations are realized by adding a heating source  $S(x, v) = H(x)G(v)$  to the right hand side of the gyro-kinetic equation, with a radial profile

$$H(x) = \sqrt{\frac{\alpha}{\pi}} \cdot \begin{cases} e^{-\alpha(x+x_H)^2} & x < \text{SFR} \\ 0 & x \in \text{SFR} \\ -e^{-\alpha(x-(L_x-x_H))^2} & x > \text{SFR}, \end{cases} \quad (1)$$

where  $x$  is the local radial coordinate,  $L_x$  is the radial size of the computational domain, and  $x_H$  denotes the position of the source. The function  $H(x)$  is shown in Fig. 1 and represents a source-sink model with a Gaussian heating profile situated at the inner edge, and an identical cooling profile at the outer edge. The two parameters  $\alpha$  and  $x_H$ , defining the width and the position of the heating profile, are  $\alpha = 0.04$  and  $x_H = 10$ . The length scales above, as well as all length scales in the direction perpendicular to the magnetic field connected with the computational domain, are normalized to the ion Larmor radius  $\rho_i = m_i v_{th}/eB_0$ , where  $m_i$  is the ion mass,  $v_{th} = \sqrt{2T_i/m_i}$  is the thermal velocity,  $e$  is the unit charge, and  $B_0$  is the magnetic field on the axis. Note that the thermal

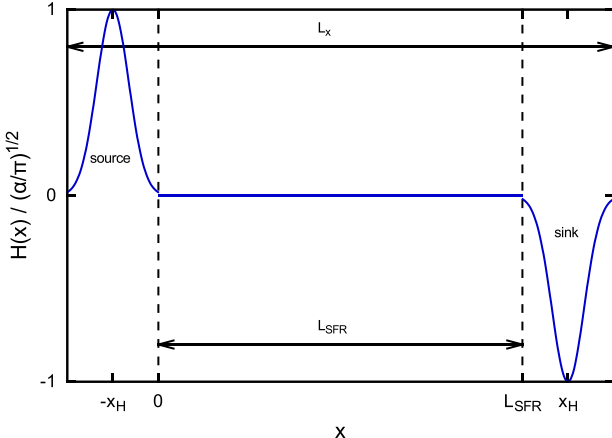


FIG. 1. Radial dependence of the heating profile used in flux driven simulations.

velocity used in the normalization contains a  $\sqrt{2}$  and is distinct from the more frequently used sound speed  $c_s = \sqrt{T_e/m_i}$ . The velocity ( $v$ ) dependence of the source  $G(v)$  is given by

$$G(v) = \Delta S \left( \frac{v^2}{v_{th}^2} - \frac{3}{2} \right) F_M, \quad (2)$$

where  $\Delta S$  is a constant that determines the strength of the source, and  $F_M$  is the Maxwell background distribution. The velocity space dependence is chosen such that  $S(x, v)$  represents an energy, but not a density or momentum source.

Between the source on the inner edge and the sink on the outer edge, a Source Free Region (SFR) exists, and it is the turbulence in this region that will be studied in this paper. The heat flux supplied to this region can be controlled by changing the source amplitude  $\Delta S$ , and the average of the resulting temperature perturbations provides information on the stationary temperature gradient. This average will be denoted by  $\langle \langle \dots \rangle \rangle$ , indicating an average over both the volume of the source free region as well as over a suitably long time interval. The flux driven data shown below are obtained with radial periodic boundary conditions, but Dirichlet boundary conditions (not presented here) have been examined and yield the same results. The flux driven results, therefore, are independent of the choice of the boundary conditions. Two sets of flux driven simulations have been performed with a radial extent for the source free region of  $L_{SFR} = 80$  and  $L_{SFR} = 160$ , respectively. For the cases  $L_{SFR} = 80/160$ , a total number of 240/400 radial grid points are used, with  $L_x = 120/200$ . The larger simulation domain ( $L_{SFR} = 160$ ) was used, because boundary effects due to the heating source cannot be completely neglected in the case of the smaller domain ( $L_{SFR} = 80$ ). These flux driven simulations are compared with the gradient driven simulations that have a radial domain size equal to the source free region of the smaller case, i.e.,  $L_x = 80$ . To have equal resolution, 160 radial grid points have been used in the gradient driven simulations. All simulations use  $N_s = 24$  grid points along the magnetic field,  $N_\mu = 12$  grid points for the magnetic moment, and  $N_{v\parallel} = 32$  points for the parallel velocity. The maximum resolved poloidal wave vector normalized to the ion Larmor radius is  $k_\theta \rho = 1.4$ . The case with  $L_{SFR} = 80$  and the gradient driven turbulence use  $N_m = 19$  toroidal modes, whereas the case with  $L_{SFR} = 160$  uses  $N_m = 37$  modes. The larger number of toroidal modes in the latter case means that the computational domain perpendicular to the magnetic field in which no source is applied is of equal size in the radial and binormal direction, also for the larger case ( $L_{SFR} = 160$ ). In the gradient driven flux tube simulations, the ion temperature gradient length  $R/L_T$  has been varied from 5.0 to 10.0 in order to obtain similar heat fluxes compared with the flux driven simulations. All temporal averages are calculated using a time interval of at least  $1 \times 10^3 R/v_{th}$  within the stationary state. For the low heating rates, times series up to  $5 \times 10^3 R/v_{th}$  was examined to get proper statistical and spectral results.

In Section III, results of the smaller radial box ( $L_{SFR} = 80$ ) are sometimes presented as a function of the

heating amplitude  $\Delta S$ , rather than the averaged radial ion heat flux  $\langle\langle Q_i \rangle\rangle$ , with

$$Q_i = \frac{1}{n_0 T_0 \rho_*^2 v_{th}} \int d^3 v v_{Er} \frac{1}{2} m v^2 f, \quad (3)$$

where  $v_{Er}$  is the radial component of the fluctuating  $E \times B$  velocity, and  $f$  is the perturbed distribution function. The heat flux is normalized using gyro-Bohm units  $Q_{GB} = n_0 T_0 \rho_*^2 v_{th}$ , where  $n_0$  and  $T_0$  are the background density and temperature. The two quantities  $\Delta S$  and  $\langle\langle Q_i \rangle\rangle$  are, however, directly related, and for clearness, Table I gives the averaged heat flux as a function of the heating for all chosen heating amplitudes.

In the flux driven simulations, the time averaged temperature gradient  $\langle\langle R/L_T \rangle\rangle$  is given by the sum of an imposed background temperature ( $T_0$ ) gradient length  $R/L_{T0}=3$  and the temperature perturbations ( $T$ ) due to the perturbed distribution

$$\left\langle \left\langle \frac{R}{L_T} \right\rangle \right\rangle = -\frac{1}{\rho_* T_0} \left\langle \left\langle \frac{\partial T}{\partial x} \right\rangle \right\rangle + \frac{R}{L_{T0}}. \quad (4)$$

Note that the  $\rho_*$  in this equation is related to the normalization of the spatial coordinate  $x$ , and  $R/L_T$  is positive for a negative radial temperature gradient. Error bars, in the case they appear for a volume and time averaged quantity  $\langle\langle \dots \rangle\rangle$ , are calculated by determining the time averages of several temporal subsets of the volume average. The standard deviation of these subset mean values provides the error estimate.

### III. NUMERICAL RESULTS

#### A. Flux-gradient relation

Fig. 2 compares the heat flux for gradient and flux driven simulations. The gradient driven simulations (blue squares) have a nonlinear threshold in the temperature gradient  $R/L_T = 6$ . Although this value is equal to the threshold given in Ref. 2, this is misleading. The circular geometry used in this paper yields higher heat fluxes compared with the  $\hat{s} - \alpha$  geometry, consistent with a lower nonlinear threshold. Indeed, linearly interpolating the heat flux obtained for  $R/L_T > 6$ , one obtains a nonlinear threshold  $R/L_T = 4.9$ . A threshold value of  $R/L_T = 6 > 4.9$  is obtained because the heat flux does not go to zero when the threshold is approached from above. Rather, the heat flux has a finite value at the nonlinear threshold. Below  $Q_i \approx 10$ , no stationary gradient driven simulation is obtained. Fig. 3 shows time traces of  $Q_i$  for GD simulations at the nonlinear threshold. The simulation data with  $R/L_{T_i} = 6.1$  (green), which represents a situation close to the threshold from above, yield a finite heat flux of  $\langle\langle Q_i \rangle\rangle \approx 10$ .

TABLE I. Source amplitudes  $\Delta S$  and corresponding average heat flux  $\langle\langle Q_i \rangle\rangle$  for the performed flux driven simulations.

$\Delta S$	Low heating				High heating					
	4	8	12	20	36	44	52	72	88	108
$\langle\langle Q_i \rangle\rangle$	1.1	3.0	5.0	9.1	15.8	18.5	21.0	26.4	30.3	35.5

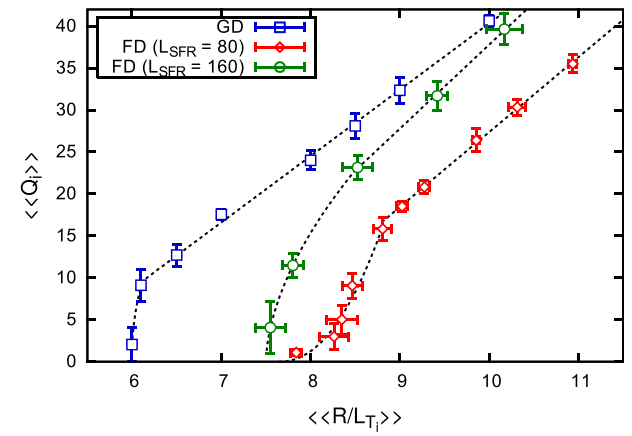


FIG. 2. Heat flux  $\langle\langle Q_i \rangle\rangle$  in units  $n_0 T_0 \rho_*^2 v_{th}$  as a function of the temperature gradient  $\langle\langle R/L_T \rangle\rangle$  for the gradient driven (blue squares) and flux driven turbulence. Both the results of the smaller domain  $L_{SFR} = 80$  (red diamonds) and the larger domain  $L_{SFR} = 160$  (green circles) are shown. The error bars give the statistical error only.

In the case of  $R/L_{T_i} = 6.0$  (blue), the system evolves into a state where turbulent transport is strongly reduced with  $\langle\langle Q_i \rangle\rangle \approx 2$ . Zonal flows develop that are sufficiently strong to quench the turbulence. The possible reason why this phenomenon has been overlooked so far is that, close to the threshold, the quenching of the turbulence often occurs after a relatively long time (after  $1500 R/v_{th}$  for the blue data in Fig. 3). Furthermore, the dissipation necessary to obtain a numerically stable solution must be sufficiently small. The important role of numerical dissipation is clarified by the red time series in Fig. 3. Reducing the numerical dissipation leads to an almost fully quenched heat flux with  $\langle\langle Q_i \rangle\rangle \approx 0.7$ . This result also holds for gradient driven simulations with  $R/L_{T_i} < 6.0$ . A heat flux that is directly related to the numerical dissipation has to be considered unphysical within the model assumptions. Consequently, for the collisionless Cyclone base case, the heat flux is considered to be zero for  $R/L_{T_i} = 6.0$ . Therefore, it is concluded that the flux tube simulations cannot describe transport in the case where the supplied heat flux is below a threshold value ( $Q_i < 10$ ). It is noted that the threshold value given above is certainly of experimental

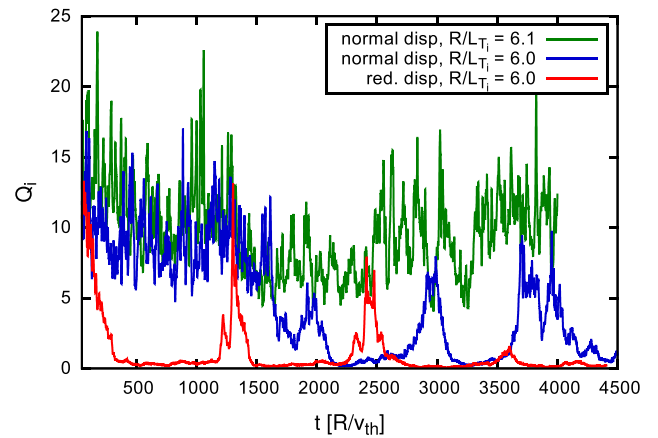


FIG. 3. Time traces of the heat flux  $Q_i$  for GD simulations at the nonlinear threshold. The blue and green simulation data are obtained with numerical dissipation used throughout the paper. The red data are obtained with reduced numerical dissipation.

relevance. Further details can be found in Ref. 5. Below, a heat flux below the threshold  $Q < 10$  will be referred to as low heating, whereas  $Q > 10$  is referred to as a high heating case.

The results of the flux driven simulations are given in Fig. 2 by the diamonds (red) and circles (green) for the small and large radial domain cases, respectively. The difference between the two reflects the influence of the source in the boundary region. In the case of the large radial domain, the boundary effects have been removed by averaging over only part of the source free region, and these simulations, therefore, represent the flux gradient relation accurately. For more details on the averaging, the reader is referred to Section III D of this paper. The results for the flux and gradient driven transport do not agree even though both are calculated in the local limit with the same underlying model. The flux driven simulations have a reduced heat flux compared with the gradient driven simulations, as well as a higher non-linear threshold. For sufficiently high heat flux, the flux driven model with  $L_{SFR} = 160 \rho_i$  approaches the GD data. This discrepancy will be shown below (Section III D) to be related to the formation of structures in the temperature profile.

## B. Statistical and spectral analysis

In this section, the statistical and spectral properties of the turbulent heat flux  $Q_i$  and temperature gradient  $R/L_T$  are discussed using the probability density function (PDF) and the power spectrum. The PDF is normalised to unity, and is based on measurements in the stationary phase and source free region. Unless explicitly stated otherwise, the results are based on the simulations with  $L_{SFR} = 80$ .

Fig. 4 shows the PDF ( $R/L_{T_i}$ ) of two gradient driven (squares and diamonds) and two flux driven (circles and triangles) simulations. Both distributions of the gradient driven case are in good agreement with a Gaussian distribution represented by the dashed lines. This applies to all distributions of the gradient driven simulations presented in this paper. Also, the PDF of the flux driven turbulence in the high heating case ( $\Delta S = 88$ ) is close to a Gaussian

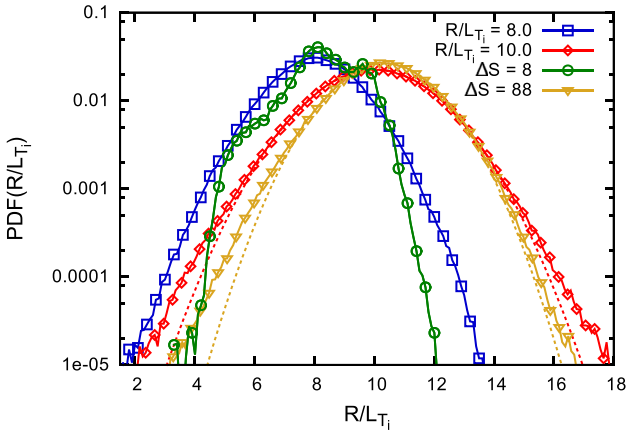


FIG. 4. PDF( $R/L_{T_i}$ ) for two flux driven simulations with  $\Delta S = 8$  (green circles) and  $\Delta S = 88$  (yellow triangles), as well as two gradient driven simulations with  $R/L_{T_i} = 8$  (blue squares) and  $R/L_{T_i} = 10$  (red diamonds). The dashed lines in the graph represent a Gaussian distribution.

distribution, i.e., the statistics of the fluctuations in  $R/L_{T_i}$  are similar to the gradient driven turbulence in this case. This is consistent with the Gaussian distribution reported in Ref. 6. A clear deviation from a Gaussian distribution, however, is present in the low heating case ( $\Delta S = 8$ ). The PDF exhibits several maxima, and the temperature gradient distribution is not symmetric around the maximum. Other simulations in the low heating region ( $\Delta S = 4, 8, 12$ ) exhibit similar inhomogeneous distributions.

The PDFs of the flux driven cases have the same lower limit  $R/L_{T_i} \sim 3 - 4$ , somewhat larger than the lower limit of the gradient driven cases  $R/L_{T_i} \sim 2$ . It follows that the gradient length in the flux driven case is always above the linear threshold, and mostly above the non-linear threshold, different from the results reported in Ref. 7. The lower limit in the flux driven case might be related to the linear threshold of the ion temperature gradient (ITG) mode.<sup>6</sup>

The distributions of  $Q_i$  are shown in Fig. 5 and differ from a Gaussian distribution for both flux as well as gradient driven turbulence. This is expected, since the heat flux is given by two cross-correlated quantities  $\langle \delta T \delta v \rangle$ . Even if both  $\delta T$  and  $\delta v$  are Gaussian distributed, their product does not necessarily need to have the same distribution.<sup>7,8</sup> Again, the distribution of the high heat flux driven case ( $\Delta S = 72$ ) is similar to the gradient driven case. At low heating power, the PDF ( $Q_i$ ) of the flux driven case, however, is positively skewed and exhibits a large tail. These are indicators of intermittent and bursty transport.<sup>7,9,10</sup> The degree of intermittency can be quantified by determining the third and fourth moment of the distribution, referred to as skewness  $\gamma$  and flatness  $k$ .<sup>11</sup> Both quantities are zero for a Gaussian distribution, and consequently, large  $\gamma$  and  $k$  indicate an intermittent behaviour. Fig. 6 shows  $\gamma$  and  $k$  as a function of the averaged heat flux  $\langle \langle Q_i \rangle \rangle$ . For heat fluxes  $\langle \langle Q_i \rangle \rangle > 10$ , the data of the flux and gradient driven cases overlay, again showing that the statistics of the two models is the same, provided the heat flux is large enough. Furthermore, it is shown that the two domain sizes in the flux driven case ( $L_{SFR} = 80$  and  $L_{SFR} = 160$ ) yield the same result. It is noted, however, that due to the higher nonlinear threshold of the temperature gradient in the flux driven case, no overlay of the data is

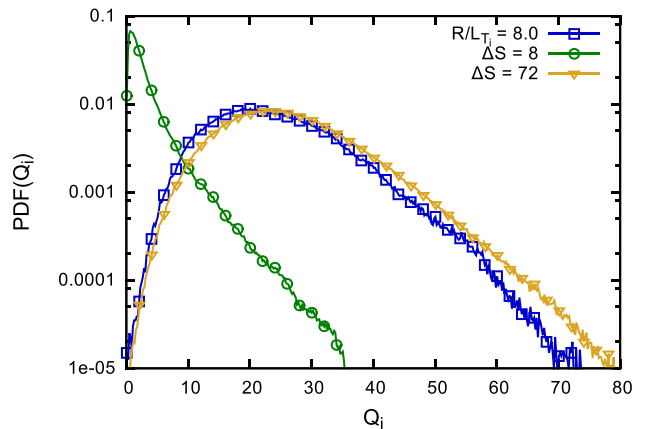


FIG. 5. PDF( $Q_i$ ) for flux driven case with  $\Delta S = 8$  (green circles) and  $\Delta S = 72$  (yellow triangles) as well as a gradient driven case with  $R/L_{T_i} = 8$  (blue squares).

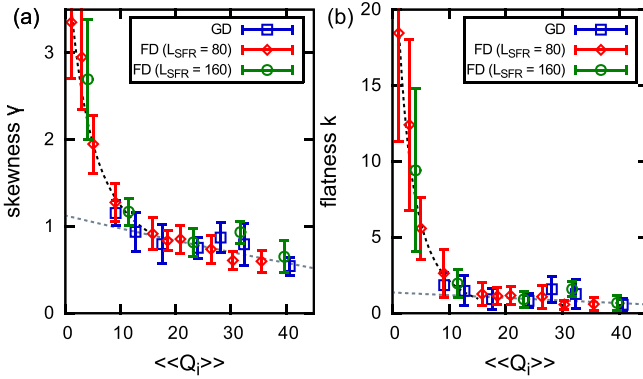


FIG. 6. Skewness  $\gamma$  and flatness  $k$  as a function of the average heat flux  $\langle\langle Q_i \rangle\rangle$  for gradient-driven (red diamonds) and flux driven turbulence. For the flux driven case, both the results of the small computational domain gradient-driven (blue squares),  $L_{SFR} = 80$  (red diamonds) and the large computational domain  $L_{SFR} = 160$  (green circles) are shown.

obtained if  $\gamma$  and  $k$  are plotted as a function of  $R/L_{T_i}$ . The obtained skewness and flatness in the high heating case  $\gamma \approx 0.5\text{--}1.1$  and  $k \approx 0.6\text{--}1.2$  are in good agreement with the values obtained in Ref. 12 for local gradient driven simulations. In contrast to Ref. 12, however,  $\gamma$  and  $k$  decrease with increasing heat flux (temperature gradient) indicating that transport becomes less bursty at higher heat fluxes (temperature gradients). A transition to a significantly higher skewness and flatness occurs when reducing the heat flux to values  $\langle\langle Q_i \rangle\rangle < 10$  reflecting a strong intermittency at low heat fluxes. The obtained values  $\gamma \approx 0.9\text{--}3.4$  and  $k \approx 1.2\text{--}18.0$  for these low heat fluxes are larger than those reported in Ref. 13 for global flux driven simulations. It should be noted that there is no data for the gradient driven simulations in these low heat flux cases. As pointed out above, for these heating powers, no stationary gradient driven simulation can be obtained. It is concluded that the gradient driven flux tube model breaks down for those cases in which the transport is strongly intermittent.

In order to characterize the dynamics of the heat flux and also the power spectrum

$$P(\omega) = |\hat{Q}_i(\omega)|^2, \quad (5)$$

of  $Q_i$  is computed, where

$$\hat{Q}_i(\omega) = \frac{1}{\sqrt{2\pi}} \int Q_i(t) e^{i\omega t} dt, \quad (6)$$

is the Fourier transform of the heat flux time trace.<sup>10</sup> The power spectrum is often discussed in relation to the Self-Organized-Criticality (SOC) model,<sup>14</sup> which is applied in the description of various natural systems, e.g., sand piles, earth quakes, astro-physical plasmas, as well as turbulent transport in tokamak plasmas. A main characteristic of SOC dynamics is the occurrence of avalanches exhibiting all length and time scales. Thus, transport events are scale invariant and self-similar. This self-similarity leads to a power law scaling in the  $P(\omega)$  spectrum. Fig. 7 shows  $P(\omega)$  for both gradient and flux driven transport. Power law regions exist for gradient driven turbulence, as well as for high heat flux driven turbulence. The typical value of the power of the SOC systems

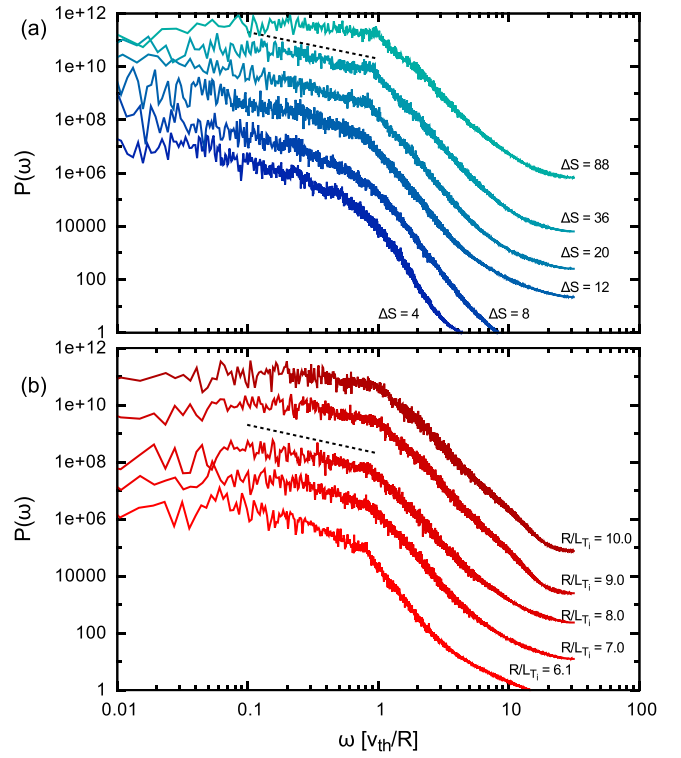


FIG. 7. Radial averaged power spectra of the heat flux  $\langle P(\omega) \rangle_x$  for flux driven (a) and gradient driven (b) turbulence as a function of the frequency (normalized to  $v_{th}/R$ ). The different spectra are vertically shifted with respect to each other in order for the curves not to overlap. The typical  $1/\omega$ -power law is indicated by the black dashed lines.

$\alpha \approx 1$  (black dashed lines in Fig. 7) is present in the mid range frequencies, where the values for the power are in the  $\alpha = 1.5\text{--}0.5$  range. The decrease of  $\alpha$  with higher heating power or temperature gradient means that higher frequencies are present in the dynamics of the heat flux.<sup>12</sup> The sharp transitions from the  $\alpha \approx 1$  scaling to a higher exponent can be attributed to a minimal pulse time scale, with the spectrum above the transition frequency describing the pulse shape.<sup>15</sup> This transition frequency is shifted to higher values for increasing heat flux, respectively, for increasing temperature gradient,<sup>7</sup> and has values in the range  $6.2\text{--}16.0 v_{th}/R$ . The power spectra of flux driven transport for the low heating cases, and especially for  $\Delta S = 4, 8$ , are rather curved. Clear power law regions, present over at least one decade, which are separated by sharp transitions, do not appear in these cases, in contrast to the original formulation of the SOC model in the limit of  $S \rightarrow 0$ .<sup>16</sup> However, recalling the intermittent character of the heat transport for the low heating case observed in the PDF ( $Q_i$ ), this result can be expected since intermittency and strict self-similarity are mutually exclusive.<sup>10,11,17</sup> For a proper discussion of SOC like behaviour, correlation diagnostics, R/S-analysis, and distributions of avalanche sizes and times need to be studied (see Refs. 12 and 15). This is beyond the scope of this paper.

### C. Avalanche dynamics

In this section, the low heat flux driven case ( $\langle\langle Q_i \rangle\rangle < 10$ ), which shows strong intermittency and has no counterpart in gradient driven turbulence, is investigated in

detail. The low heat flux driven turbulence is found to be dominated by avalanches, a phenomenon which has been reported earlier for flux-driven ITG turbulence in gyro-fluid simulations<sup>18,19</sup> as well as global gyro-kinetic simulations.<sup>7,20–22</sup> Fig. 8 shows the heat flux as a function of the radial coordinate and time for two flux driven simulations with  $\langle\langle Q_i \rangle\rangle < 10$ . The avalanches in this figure are visible as radially extended and clearly distinguishable coherent structures. The transport events are spatially organized and their temporal distribution is inhomogeneous, which reflects the intermittent character. These properties essentially separate the low heat ( $\langle\langle Q_i \rangle\rangle < 10$ ) flux driven case from the higher heat flux driven case as well as from the gradient driven turbulence. Also shown in Fig. 8 is the  $E \times B$  shearing rate connected with the zonal mode  $\omega_{E \times B}$  (toroidal mode  $n = 0$ )

$$\omega_{E \times B} = \frac{1}{B} \frac{\partial^2 \phi}{\partial x^2}, \quad (7)$$

where  $\phi$  is the electro-static potential. Below, the spatial organization, intermittency, and the appearance of profile effects are discussed.

### 1. Spatial organization

In Figs. 8(a) and 8(b), some observations on the spatial organization can be made. Large scale avalanches are initiated at specific positions. Against expectations, these positions are not located close to the heat source, i.e., at the boundary of the computational domain, but are located at several positions in the source free region. Since the avalanches have straight propagation fronts, their propagation is ballistic.<sup>23</sup> Fitting the propagation fronts in the  $x - t$  plane, velocities in the range of

$v \approx 2 - 12 \rho_i v_{th}/R$  are obtained, in good agreement with Refs. 20 and 22, wherein propagation speeds of order  $\sim \rho_* v_{th}$  are reported. In addition, it is found that the propagation speed is independent of the heating rate within the error bars, and thus appears to be a universal quantity. Avalanches propagate up and down the gradient, which is essentially a consequence of the joint reflection symmetry<sup>16,24</sup> of the underlying local transport mechanism. As a consequence, avalanches propagate symmetrically to the initial position leading to “V”-shaped transport events in the spatio-temporal representation. Additionally, the propagation direction and sign of the  $E \times B$  shearing rate are correlated (see also Refs. 20, 22, and 25). The avalanches propagate over a radial distance  $\sim 60 \rho_i$  (measured from the minimum position up the gradient position to the maximum down the gradient position), which exceeds the typical turbulent correlation length of  $l_c \sim 5 \rho_i$ ,<sup>26</sup> as well as the length scale over which turbulence spreading is important.<sup>27–29</sup> In Fig. 8, a restriction of avalanches to certain radial regions with the same characteristic length can be observed. The resulting spatial organization of turbulence is related to the formation of  $E \times B$ -staircases, and will be addressed in Section III D. It is noted that a spatial organization of turbulence is not present in the high heating flux driven or gradient driven turbulence. Rather, the turbulence is homogeneous in these cases.

### 2. Intermittency

The intermittent character of turbulent transport in the low heat flux driven case, which is anticipated by the high skewness and flatness (Fig. 6), is visible in the time traces of the heat flux  $Q_i$  of Fig. 9. The temporal behaviour is different from the high heat flux driven case as well as the gradient driven turbulence, where  $Q_i$  is fluctuating homogeneously

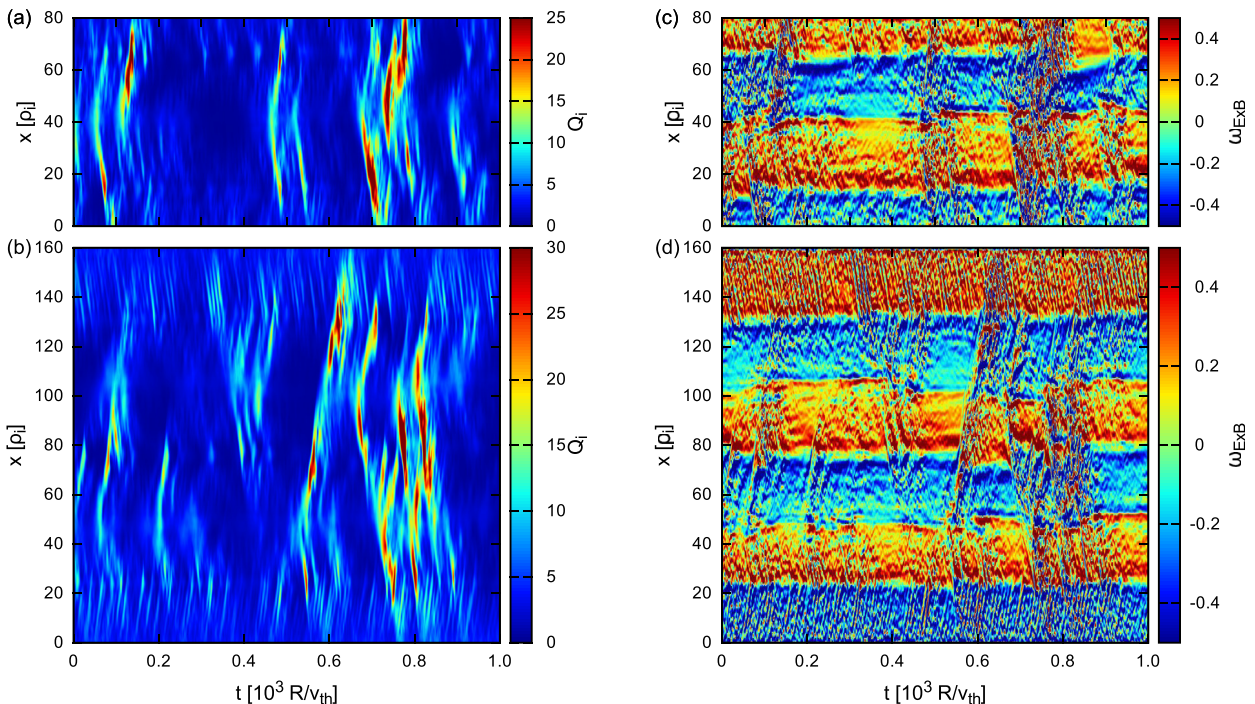


FIG. 8. Spatio-temporal evolution of the heat flux (a) and (b) as well as the shearing rate (c) and (d). The plots at the top correspond to flux-driven simulation with  $L_{SFR} = 80$ ,  $\langle\langle Q_i \rangle\rangle = 3.0$ , and  $(\Delta S = 8)$ . The larger boxes at the bottom represent the double size flux-driven simulation ( $L_{SFR} = 160$ ) with a slightly higher heating rate  $\langle\langle Q_i \rangle\rangle = 4.4$ . All plots show only the source free region of the computational domain.

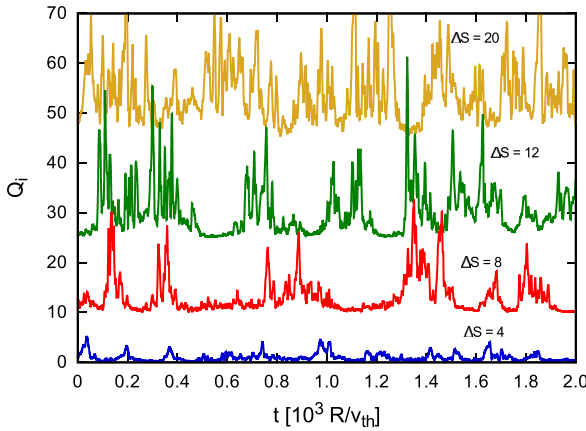


FIG. 9. Time evolution of the heat flux  $Q_i$  at the centre of the computational domain with  $L_{SFR} = 80$ . The various curves are shifted vertically with respect to each other such that they do not overlap.

in time. Two basic observations can be made. First, the avalanches are separated by quiet periods. The time scale of these quiet periods reaches up to  $\sim 500R/v_{th}$ , and thus exceeds the typical time scale of a single heat pulse  $5 - 20R/v_{th}$ . With increasing heating rate ( $\Delta S$ ), the quiet periods become shorter until they finally vanish at high heating ( $\Delta S \geq 36$ ,  $\langle\langle Q_i \rangle\rangle > 10$ ). Second, the active turbulent periods, separated by the quiet periods, change with increasing heat flux. An evolution from single avalanche events ( $\Delta S = 4$ ), via avalanche cascades ( $\Delta S = 8, 12, 20$ ), to continuous turbulence ( $\Delta S > 20$ ) can be observed. Therefore, there is a fluent transition from a temporal inhomogeneous turbulent state to fully developed turbulence. Finally, it is noted that the time scale of a heat pulse approximated by measuring the width of a single spike in Fig. 9 agrees with the transition frequency found in the power spectrum analysis in Section III B.

### 3. Profile effect

To examine the propagation of an avalanche, it is worthwhile to split the temperature gradient  $R/L_{T_i}$  and the shearing rate  $\omega_{E \times B}$  into a temporal averaged and a fluctuating part

$$R/L_{T_i} = \langle R/L_{T_i} \rangle_t + \delta(R/L_{T_i}). \quad (8)$$

Fig. 10(a) shows the outward propagating front of a heat avalanche for three successive time steps. A local transport process causes the flattening of the temperature gradient, thus producing a “valley” in  $\delta(R/L_{T_i})$ , while the outward propagation of heat steepens the gradient further outwards. In the case of marginal stability, this steepening of the gradient triggers turbulence resulting in a domino effect.<sup>24</sup>

Avalanches lead to fluctuations in the  $E \times B$  shearing rate, as shown in Figs. 8(c) and 8(d) by the tilted structures that correspond to the avalanches in the left panels (a) and (b). The amplitude of  $\delta(\omega_{E \times B})$ , which is shown in Fig. 10(c) for one avalanche event, can reach values of the order  $\sim v_{th}/R$ , well in excess of the maximum temporal averaged shearing rate  $\langle\omega_{E \times B}\rangle_t \sim 0.4$ , and is large compared to the typical linear growth rate ( $\gamma_{lin} \sim 0.2 - 0.4$  for  $R/L_{T_i}$

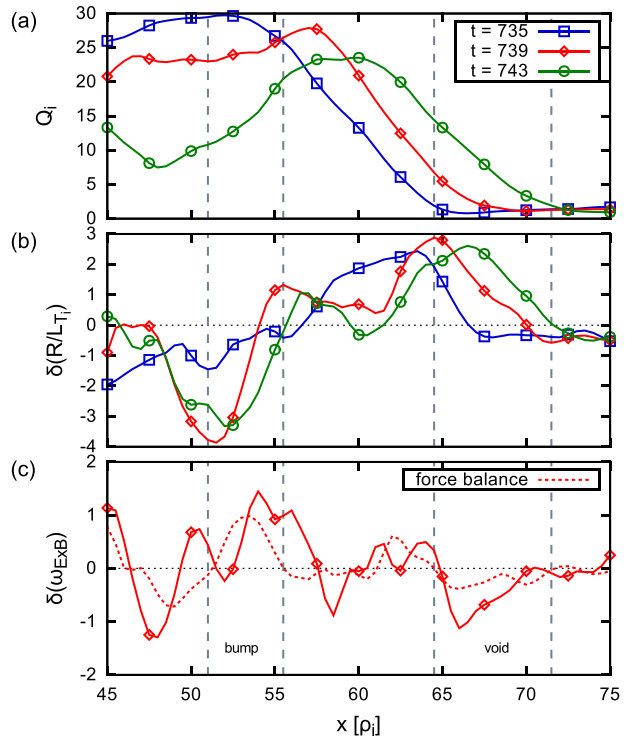


FIG. 10. Outward propagating avalanche front for a flux driven simulation with  $\Delta S = 8$ . The profiles of the heat flux (a), the fluctuation part of the temperature profile (b), and the shearing rate (c) are shown for successive time points ( $735 - 743R/v_{th}$ ).

$\sim 6 - 9$ ). The profile of  $\omega_{E \times B}$  during an avalanche can be partly understood through the occurrence of the pressure gradient in the ion radial force balance, i.e.,  $en_i \partial \phi / \partial x = -\partial p_i / \partial x$ , where  $p_i$  is the ion pressure. This yields a shearing rate

$$\begin{aligned} \omega_{E \times B} = \frac{1}{2} & [\partial_x R/L_{T_i} + \partial_x R/L_{n_i} \\ & + \rho_* \cdot (R/L_{n_i})^2 - \rho_* \cdot R/L_{T_i} \cdot R/L_{n_i}]. \end{aligned} \quad (9)$$

The last two terms in the equation above vanish in the local limit  $\rho_* \rightarrow 0$ . Furthermore, the second term is small for ITG turbulence with adiabatic electrons, resulting in a shearing rate

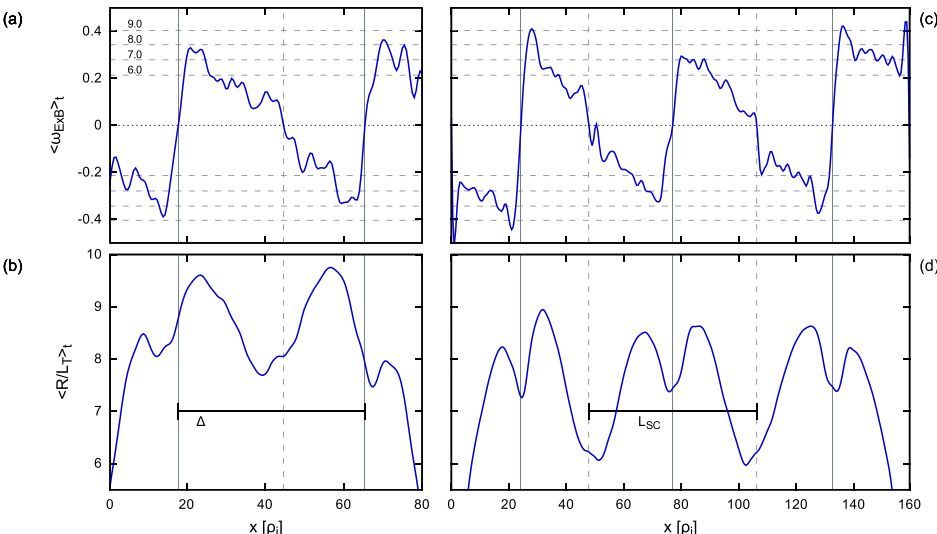
$$\omega_{E \times B} = \frac{1}{2} \partial_x R/L_{T_i}, \quad (10)$$

that is directly related to the temperature profile through the second derivative. The shearing rate related to the pressure gradient is shown by dashed lines in Fig. 10(c). It cannot reproduce the whole structure of the simulated shearing rate, and therefore, the contribution of the plasma rotation in the force balance cannot be neglected. Nevertheless, it shows the bounding of the propagation front in  $Q_i$  by a bump and a void in the shearing rate. A similar structure has also been reported in Ref. 20. Note that such a bounding is present for every avalanche event as can be seen in Figs. 8(c) and 8(d), where all avalanches are represented by both a blue as well as a red tilted line.

## D. Formation of $E \times B$ -staircases

The spatial organisation of avalanches and the restriction of transport events to certain regions defining a typical avalanche length are related to the formation of spatial patterns in the profile of the shearing rate (Figs. 8(c) and 8(d)), known as  $E \times B$  staircases.<sup>30,31</sup> These patterns are stationary during the entire simulation (at least up to  $5 \times 10^3 R/v_{th}$ ). The appearance of these patterns in our simulations means that a global description of the turbulence is not a necessary ingredient for their formation. It is noted, however, that in the simulations presented here, the staircases do not move radially. One might speculate therefore that the radial motion observed in Ref. 31 is due to global (profile) effects.

Since the pattern is temporal stable, the specific shape is well expressed by the temporal average  $\langle \cdot \rangle_t$  shown in Fig. 11. Doubling the box size from  $L_{SFR} = 80$  (a) to  $L_{SFR} = 160$  (c) doubles the number of staircases in the box and, therefore, does not change the radial extent of the structures. Thus, the radial extent of the patterns is not related to the boundary conditions. Which physics sets the size of the structure is at present unknown. The shearing rate has a sawtooth like pattern that repeats itself periodically. The maximum value obtained within the pattern does not vary with the heating rate and is in the range of  $\omega_{ExB} = 0.3 - 0.4 v_{th}/R$ . The latter magnitude represents a strong mean shear flow that is capable of stabilizing the turbulence, especially for lower temperature gradient lengths. Within the periodic  $E \times B$  shear pattern, a steep step occurs in the shearing rate, referred to as bipolar shear-layers in Ref. 31. Avalanches are initiated at the position where the shearing rate changes sign slowly with radius (i.e., not at the zero crossing in the bipolar shear layer), and tend to stop at the positions of the bipolar shear layer, resulting in an upper limit of the radial extent of an avalanche for most of the events. Therefore, the radial extent of the periodic structures and avalanches is determined by the same meso-scale length  $\Delta = 50 - 70 \rho_i$ , which is slightly larger than the scale reported in Refs. 30 and 31. This meso-scale length is significantly larger than the turbulent correlation length  $l_c \sim 5 \rho_i$ , which is also the length scale on which turbulence spreading occurs,<sup>29</sup>



but smaller than the computational domain or system size. The temporal averaged profiles of the temperature gradient length in Figs. 11(b) and 11(d) show the same periodicity as the staircase pattern. Large temperature gradients are observed at the position of the bipolar shear layers. The increase in  $R/L_T$  at this position is consistent with the  $E \times B$  shear stabilization of turbulent transport, which occurs when the  $E \times B$  shearing rate is comparable to the linear growth rate of the most unstable mode.<sup>32</sup> Figs. 11(a) and 11(c) show the linear growth rates (horizontal dashed lines) for temperature gradient lengths  $R/L_{T,i} = 6 - 9$ . With a maximum  $E \times B$  shearing amplitude  $\omega_{ExB} = 0.3 - 0.4 v_{th}/R$ , a maximum temperature gradient length of 8–9 is expected, in good agreement with the simulations that use the larger computational domain ( $L_{SFR} = 160$ ). (The agreement for the smaller computational domain is less good, due to boundary effects.) It is noted also that the central temperature corrugation reflects the symmetric shape of one shear layer. At the zero crossing of the  $E \times B$  shearing that does not correspond to the bipolar shear layer, the temperature gradient is equal to the nonlinear threshold, in agreement with the results of Ref. 31. The enhancement gradient length at the bipolar layer explains the upshift in the flux gradient relation for the low heated flux driven cases compared with the gradient driven turbulence. Therefore, the enhanced nonlinear threshold of the flux driven case is a consequence of the formation of the  $E \times B$ -staircase pattern. Fig. 12 shows the approximation of the shear profile from the pressure gradient using the time averaged temperature gradient. Although the  $E \times B$  shear profile obtained from the pressure gradient in the force balance exhibits some periodicity, it cannot reproduce the specific shape of the staircase pattern. Thus, the temporal stable  $E \times B$  pattern is connected with a temporal stable plasma rotation.

At several points, in this paper, it has been pointed out that although the statistics of the turbulence is well described in simulations with the smaller computational domain  $L_{SFR} = 80$ , not all quantities can be obtained with the desired accuracy due to the effect of the boundary conditions. If one assumes that the source can influence the turbulence over a length scale equal to the correlation length of the turbulence, and if one assumes a correlation length of the order  $\sim 5\rho_i$ ,

FIG. 11. Time averaged profiles (over  $10^3 R/v_{th}$  within the stationary state) of the shearing rate  $\omega_{ExB}$  ((a) and (c)) and the temperature gradient length ((b) and (d)). The profiles on the left correspond to a flux driven simulation with the smaller computational domain  $L_{SFR} = 80$  and  $\langle \langle Q_i \rangle \rangle = 3.0$  ( $\Delta S = 8$ ), while on the right, a simulation with the large computational domain ( $L_{SFR} = 160 \rho_i$ ) with  $\langle \langle Q_i \rangle \rangle = 4.4$  is shown. Horizontal dashed lines specify the linear growth rate of ITG denoted by its background temperature gradient length.

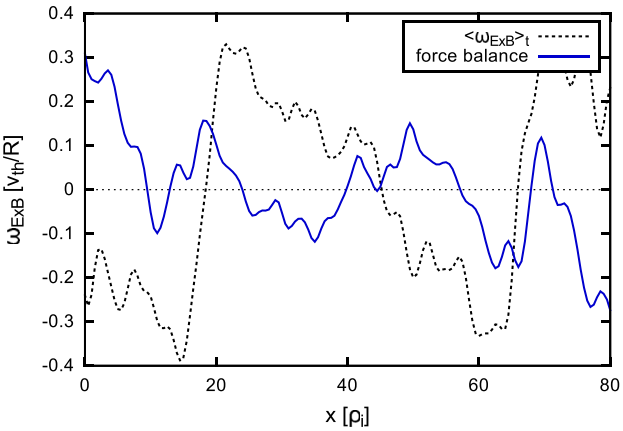


FIG. 12. Radial profile of the shearing rate  $\omega_{ExB}$  and the shearing rate calculated from the pressure gradient in the radial force balance, for a flux driven simulation ( $L_{SFR} = 80$ ) with  $\Delta S = 8$  ( $\langle\langle Q_i \rangle\rangle = 3.0$ ).

the volume of the source free region influenced by the non-physical implementation of the source is approximately 12.5% for the  $L_{SFR} = 80 \rho_i$  case. A non-negligible influence of the source is therefore possible in this case. For this reason, additional simulations have been undertaken with a larger box size  $L_{SFR} = 160$ . Not only does the larger interval reduce the relative magnitude of the volume affected, the quantities in the source free region are also averaged over a domain that is centered in the computational box away from the boundary layers, thereby avoiding the influence of the region affected by the source. The radial domain in which the data are obtained is denoted by  $L_{SC}$  in Fig. 11(d) and is separated from the boundary by several turbulent correlation lengths. It is extended over one staircase, and since the staircase pattern is periodic, the reduced data set is assumed to contain all the relevant physical information. The flux gradient relation of the larger computational domain shown in Fig. 2 has been obtained by analyzing the domain  $L_{SC}$  only and, therefore, represents an accurate determination of this relation compared with the results of the smaller computational domain.

Finally, it stressed that the staircases of the form visible in Fig. 11 are exclusively present in the low heating limit of flux driven turbulence. With increasing heating rate, the pattern becomes unstable and breaks up into several staircases that have a reduced life time, as shown in Fig. 13 for a flux driven simulation close to the transition to the high heating region. In the high heating case, the staircases pattern is no longer present, but is replaced by a homogeneously fluctuating shearing rate comparable to the shearing rate in gradient driven turbulence. An explanation for the disappearance of the staircase pattern could be the strong fluctuations in shearing rate induced by the turbulent transport. At sufficient high heating rate, the amplitude of these fluctuations exceeds the constant amplitude of the staircases, which might prevent their formation. However, the physical understanding of the mechanisms which are responsible for the formation of the staircases as well as their dynamics is an ongoing topic of research. A model has recently been developed based on the delay-time between drift-waves and zonal flows.<sup>33–36</sup>

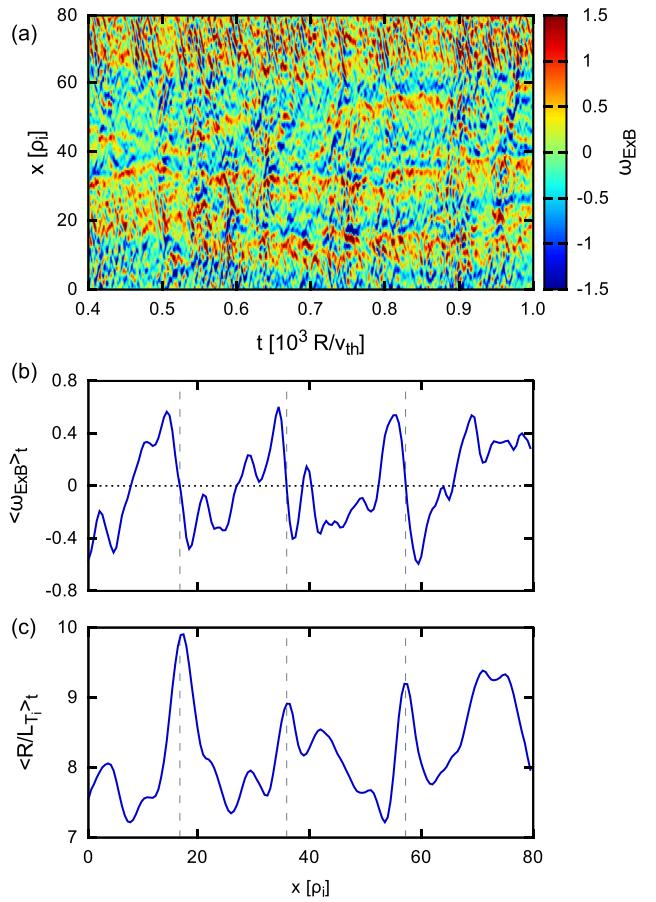


FIG. 13. Top Spatio-temporal evolution of the shearing rate ( $L_{SFR} = 80$ ) for a flux driven simulation with  $\Delta S = 20$  ( $Q_i = 9.1$ ). Also shown are the temporal averaged profiles (800 – 900  $R/v_{th}$ ) of the shearing rate  $\omega_{ExB}$  (b) and the temperature gradient length  $R/L_{T_i}$  (c). At the latter time interval, the single staircase has broken up and there are three shear layers with corresponding temperature corrugations.

#### IV. CONCLUSION

In this paper, flux and gradient driven ion temperature gradient turbulence in tokamak geometry have been compared. The same underlying gyro-kinetic model, numerical implementation, and flux tube geometry are used in both cases. In the gradient driven transport, the background temperature gradient is prescribed, and periodic boundary conditions in the plane perpendicular to the magnetic field are used. Flux driven transport is simulated through the use of a heating source.

The study reveals an important limitation of the gradient driven transport model. In the gradient driven case, the heat flux does not go smoothly to zero when the threshold is approached from above. Instead, it has a finite ion heat flux  $Q_i \approx 10$  at a nonlinear threshold  $R/L_{T_c} = 6$ . The threshold in  $R/L_T$  is significantly larger than the interpolated heat flux (Dimits) result  $R/L_{T_c} = 4.9$ . Below  $R/L_T = 6$ , no stationary fully developed turbulent state can be obtained in the gradient driven case. Consequently, the gradient driven local transport model is unable to accurately describe heat fluxes below  $Q_i < 10$ . It is noted that this value is of experimental relevance. At the threshold  $R/L_T = 6$ , the heat flux above corresponds to a heat conduction coefficient  $\chi_i = 1.67 \rho^2 v_{th}/R$ , which for Deuterium with  $T = 1$  keV,  $B = 2$  T, and

$R = 1.65$  m corresponds to  $\chi_i \approx 2 \text{ m}^2/\text{s}$  close to the values obtained under experimental conditions.

For the heat fluxes for which the gradient driven turbulence breaks down, the turbulence in the flux driven case shows intermittent behaviour and avalanches. Isolated avalanches disappear for  $Q_i > 10$ , and for these heat fluxes, the statistics of the turbulence is the same for the flux and gradient driven case. Furthermore, at sufficient high heating rates, the heat flux in the flux driven case (for  $L_{FSR} = 160 \mu\text{m}$ ) approaches the gradient driven transport at the same temperature gradient length. An additional nonlinear upshift in the temperature gradient length threshold is obtained for flux driven transport, with  $R/L_{T_c} = 7.5$ . This higher nonlinear upshift is attributed to the generation of structures in the radial temperature profile, known as staircases.<sup>30</sup> The avalanches are initiated at specific locations and have a more or less constant radial extent, in agreement with the results presented in the literature. The staircases are obtained at low heating rates, and become unstable and break up at higher heating rates. At the heat fluxes for which staircase formation is observed, no stationary gradient driven simulations can be obtained.

In this paper, it is clarified under which conditions flux and gradient driven transport yield the same results, in which the region of parameter space staircase formation is important, and for that parameters, the gradient driven model becomes inaccurate. The latter limitation is perhaps unexpected, since the flux tube model with periodic boundary conditions and a fixed temperature gradient is a consistent description of local transport, and any profile of the gradient length can be described as the sum of a background value and a periodic perturbation. Nevertheless, in the gradient driven model, the temperature gradient averaged over the radial domain is equal to the specified background value at all times. The spatially averaged temperature gradient is, therefore, not allowed to fluctuate in time. This, for instance, does not allow the averaged temperature gradient for a simulation with a specified gradient above the threshold, to fall below the threshold for a limited time interval. Finally, the reader is cautioned that the presented data are obtained by a physical reduced model, e.g., adiabatic electrons, concentric flux surfaces, and no collisions. In future works, the robustness of the observed phenomenon has to be considered in more realistic situations.

<sup>1</sup>A. J. Brizard and T. S. Hahm, *Rev. Mod. Phys.* **79**, 421 (2007).

<sup>2</sup>A. M. Dimits, G. Bateman, M. A. Beer, B. I. Cohen, W. Dorland, G. W. Hammett, C. Kim, J. E. Kinsey, M. Kotschenreuther, A. H. Kritz, L. L. Lao, J. Mandrekas, W. M. Nevins, S. E. Parker, A. J. Redd, D. E. Shumaker, R. Sydora, and J. Weiland, *Phys. Plasmas* **7**, 969 (2000).

<sup>3</sup>X. Lapillonne, S. Brunner, T. Dannert, S. Jolliet, A. Marinoni, L. Villard, T. Görler, F. Jenko, and F. Merz, *Phys. Plasmas* **16**, 032308 (2009).

<sup>4</sup>A. G. Peeters, D. Strintzi, Y. Camenen, C. Angioni, F. J. Casson, W. A. Hornsby, and A. P. Snodin, *Phys. Plasmas* **16**, 042310 (2009).

<sup>5</sup>A. B. Peeters, C. Angioni, R. Buchholz, Y. Camenen, F. J. Casson, S. R. Grosshauser, W. A. Hornsby, F. Rath, D. Strintzi, and A. Weikl,

"Gradient-driven flux-tube simulations of ion temperature gradient turbulence close to the non-linear threshold," *Phys. Plasmas* (unpublished).

<sup>6</sup>Y. Idomura and M. Nakata, *Phys. Plasmas* **21**, 020706 (2014).

<sup>7</sup>Y. Sarazin, V. Grandgirard, J. Abiteboul, S. Allfrey, X. Garbet, Ph. Ghendrih, G. Latu, A. Strugarek, and G. Dif-Pradalier, *Nucl. Fusion* **50**, 054004 (2010).

<sup>8</sup>M. Shats and H. Punzmann, *Turbulence and Coherent Structures in Fluids, Plasmas and Nonlinear Media* (World Scientific Publishing Co. Pte. Ltd., Singapore, 2006).

<sup>9</sup>O. E. Garcia, V. Naulin, A. H. Nielsen, and J. Juul Rasmussen, *Phys. Plasmas* **12**, 062309 (2005).

<sup>10</sup>R. Sánchez, D. E. Newmann, and B. A. Carreras, *Nucl. Fusion* **41**, 247–256 (2001).

<sup>11</sup>F. Uriel, *Turbulence* (Cambridge University Press, Cambridge, 2004).

<sup>12</sup>M. Mavridis, H. Isliker, L. Vlahos, T. Görler, F. Jenko, and D. Told, *Phys. Plasmas* **21**, 102312 (2014).

<sup>13</sup>S. Jolliet and Y. Idomura, *Nucl. Fusion* **52**, 023026 (2012).

<sup>14</sup>P. Bak, C. Tang, and K. Wiesenfeld, *Phys. Rev. Lett.* **59**, 381–384 (1987).

<sup>15</sup>R. Woodard, D. E. Newmann, R. Sánchez, and B. A. Carreras, *Phys. A* **373**, 215–230 (2007).

<sup>16</sup>T. Hwa and M. Kardar, *Phys. Rev. A* **45**, 7002–7023 (1992).

<sup>17</sup>V. Carbone, L. Sorriso-Valvo, E. Martines, V. Antoni, and P. Veltri, *Phys. Rev. E* **62**, R49(R) (2000).

<sup>18</sup>X. Garbet and R. E. Waltz, *Phys. Plasmas* **5**, 2836–2845 (1998).

<sup>19</sup>Y. Sarazin and Ph. Ghendrih, *Phys. Plasmas* **5**, 4214–4228 (1998).

<sup>20</sup>Y. Idomura, H. Urano, N. Aiba, and S. Tokuda, *Nucl. Fusion* **49**, 065029 (2009).

<sup>21</sup>S. Ku, C. S. Chang, and P. H. Diamond, *Nucl. Fusion* **49**, 115021 (2009).

<sup>22</sup>B. F. McMillan, S. Jolliet, T. M. Tran, L. Villard, A. Bottino, and P. Angelino, *Phys. Plasmas* **16**, 022310 (2009).

<sup>23</sup>X. Garbet, Y. Sarazin, F. Imbeaux, P. Ghendrih, C. Bourdelle, Ö. D. Gürcan, and P. H. Diamond, *Phys. Plasmas* **14**, 122305 (2007).

<sup>24</sup>P. H. Diamond and T. S. Hahm, *Phys. Plasmas* **2**, 3640 (1995).

<sup>25</sup>T. Görler, X. Lapillonne, S. Brunner, T. Dannert, F. Jenko, S. K. Aghdam, P. Marcus, B. F. McMillan, F. Merz, O. Sauter, D. Told, and L. Villard, *Phys. Plasmas* **18**, 056103 (2011).

<sup>26</sup>G. Dif-Pradalier, G. Hornung, P. Ghendrih, F. Clairet, P. H. Diamond, Y. Sarazin, L. Vermaire, J. Abiteboul, T. Cartier-Michaud, C. Ehrlacher, D. Estève, X. Garbet, V. Grandgirard, Ö. D. Gürcan, P. Hennequin, Y. Kosuga, G. Latu, P. Morel, C. Norscini, and R. Sabot, "The Plasma E × B Staircase: Turbulence Self-regulation through spontaneous flow patterning," in *42nd EPS Conference on Plasma Physics*, edited by R. Bingham, W. Suttorp, S. Atzeni, R. Foest, K. McClements, B. Goncalves, C. Silva, and R. Coelho (European Physical Society, Geneva, 2015).

<sup>27</sup>Z. Lin, *Phys. Rev. Lett.* **88**, 195004 (2002).

<sup>28</sup>R. E. Waltz, *Phys. Plasmas* **12**, 072303 (2005).

<sup>29</sup>P. Migliano, R. Buchholz, S. R. Grosshauser, W. A. Hornsby, A. G. Peeters, and O. Stauffert, *Nucl. Fusion* **56**, 014002 (2016).

<sup>30</sup>G. Dif-Pradalier, P. H. Diamond, V. Grandgirard, Y. Sarazin, J. Abiteboul, X. Garbet, Ph. Ghendrih, A. Strugarek, S. Ku, and C. S. Chang, *Phys. Rev. E* **82**, 025401(R) (2010).

<sup>31</sup>G. Dif-Pradalier, G. Hornung, Ph. Ghendrih, Y. Sarazin, F. Clairet, L. Vermaire, P. H. Diamond, J. Abiteboul, T. Cartier-Michaud, C. Ehrlacher, D. Estève, X. Garbet, V. Grandgirard, Ö. D. Gürcan, P. Hennequin, Y. Kosuga, G. Latu, P. Maget, P. Morel, C. Norscini, R. Sabot, and A. Storelli, *Phys. Rev. Lett.* **114**, 085004 (2015).

<sup>32</sup>R. E. Waltz, G. D. Kerbel, J. Milovich, and G. W. Hammett, *Phys. Plasmas* **2**, 2408 (1995).

<sup>33</sup>Y. Kosuga, P. H. Diamond, and Ö. D. Gürcan, *Phys. Rev. Lett.* **110**, 105002 (2013).

<sup>34</sup>Z. B. Guo, P. H. Diamond, Y. Kosuga, and Ö. D. Gürcan, *Phys. Rev. E* **89**, 041101(R) (2014).

<sup>35</sup>Z. B. Guo, P. H. Diamond, Y. Kosuga, and Ö. D. Gürcan, *Nucl. Fusion* **55**, 043022 (2015).

<sup>36</sup>Z. B. Guo, P. H. Diamond, Y. Kosuga, and Ö. D. Gürcan, *Phys. Plasmas* **21**, 090702 (2014).